RSC Advances

PAPER

View Article Online
View Journal | View Issue

Cite this: *RSC Adv.*, 2017, **7**, 25160

Design of 3D WO_3/h-BN nanocomposites for efficient visible-light-driven photocatalysis†

Jia Yan,[a] Jiemin Gu,[a] Xin Wang,[a] Yamin Fan,[a] Yan Zhao,[a] Jiabiao Lian,[a] Yuanguo Xu,[a] Yanhua Song,[b] Hui Xu*[a] and Huaming Li*[a]

3D WO_3 nanoparticle/h-BN nanosheet composites (WO_3/BN) have been designed and fabricated by a simple *in situ* one-step calcination method. By homogeneous dispersing WO_3 on graphene-like BN nanosheets, the as-fabricated WO_3/BN nanocomposites provided large surface area with more active sites, and a significant red shift of absorption edge from 310 nm to 800 nm containing the full visible optical spectrum absorption was realized, which was favorable for enhancing the absorption of the visible light area and taking full advantages of visible light utilization. Subsequently, the as-fabricated nanocomposites were employed for photocatalytic study under visible light illumination, and the 20% WO_3/BN sample exhibited the highest photocatalytic activity for Rhodamine B (RhB) degradation with the degradation efficiency of ~92%. Additionally, the WO_3/BN nanocomposites have the excellent degradation efficiency toward Ciprofloxacin (CIP) that was hard to be degradation under visible light illumination, which could be ascribed to the homodisperse WO_3 with more effective active sites for the target pollutants and a synergistic effect between the WO_3 and graphene-like BN. ESR and the radical trapping experiments were further conducted to study the degradation mechanism, and a possible reaction mechanism was proposed, which revealed that the greatly improved photocatalytic activity was mainly ascribed to the high electron–hole separation and transfer efficiency. Our exploration of graphene-like BN modified with WO_3 open a window for the use of other graphene-like BN based composition photocatalysis field.

Received 10th March 2017
Accepted 25th April 2017

DOI: 10.1039/c7ra02929b

rsc.li/rsc-advances

1. Introduction

For the past few years, numerous efforts have been devoted to developing effective techniques to eliminate organic pollutants due to increasingly prominent energy and environmental issues. For this purpose, photocatalytic technology has aroused much attention, which is regarded as an environmentally friendly and effective method.[1–4] Titanium dioxide (TiO_2), a typical semiconductor photocatalyst, has been reported as a promising candidate due to its chemical inertness, fantastic photocatalytic ability and nontoxicity.[5,6] Unfortunately, its wide band gap (E_g = 3.2 eV) makes it difficult to utilize solar energy except ultraviolet (UV) light,[7] which only occupies less than 5% of the solar light.[8] Moreover, low specific surface area and high recombination rate of photo-generated electron–hole pairs severely limits its applications.[9] Therefore, designing of novel, stable and effective photocatalysts with relatively high specific surface area, low recombination rate of electron–hole and high visible light use efficiency is urgently in demand.

As is known to all, photocatalysts with appropriate band gap energy is the essential condition for visible light absorption and utilization.[10,11] Tungsten trioxide (WO_3), benefitting for its narrow band gap (E_g = 2.5–2.8 eV),[12,13] good corrosion resistance, high photocorrosion resistance and physicochemical stability,[14,15] owns the advantage of excellent visible light absorption property and is considered as a hopeful visible-light-driven photocatalyst. However, the position of WO_3 conduction band (CB = 0.75 eV) is not high enough for O_2 reduction,[16] and is also faced with high recombination rate of the photo-generated electron–hole pairs,[17] leading to an unsatisfactory photocatalytic performance under visible light. Therefore, effective strategies have been taken to facilitate separation of electrons and holes, such as size and morphology controlling, noble metal loading, and semiconductors coupling.[16,18–21] WO_3/BiOCl,[22] WO_3/TiO_2,[23] WO_3/ZnO,[24] WO_3/SiO_2 [25] and other WO_3-based nanocomposites were fabricated and exhibited great potential in photo-generated electrons and holes efficient separation, demonstrating a wonderful photocatalytic activity toward the pollutions. Recently, our group demonstrated WO_3/g-C_3N_4 nanocomposites with enlarged specific surface areas and suitable band alignment, which was beneficial for light absorption and charge transportation, accounting for the higher photocatalytic activities towards

[a]School of Chemistry and Chemical Engineering, Institute for Energy Research, Jiangsu University, Zhenjiang 212013, P. R. China. E-mail: xh@ujs.edu.cn; lihm@ujs.edu.cn; Fax: +86-0511-88799500; Tel: +86-0511-88799500

[b]School of Environmental and Chemical, Engineering, Jiangsu University of Science and Technology, Zhenjiang 212003, P. R. China

† Electronic supplementary information (ESI) available. See DOI: 10.1039/c7ra02929b

methylene blue (MB) and 4-chlorophenol (4-CP) degradation than that of bare WO_3.[16] As proved, surface modification is an efficient strategy for the improvement of photocatalytic activities. And to make better use of WO_3, we devote ourselves to explore other appropriate functional elements or groups to further optimize the photocatalytic performance.

Boron nitride (BN), graphene-like material, owning to its suitable structure and fantastic properties, such as high thermal stability, good chemical stability with excellent acid and oxidation resistance, especial photoconductivity and non-toxicity, draws much attention in the application of electrical resistance, thermal conductivity, catalytic activity, and opto-electronic properties.[26–30] Also, graphene-like BN with special layered structure and large surface area, presenting outstanding durability and abundant active sites, is rationally regarded as a suitable support material in potential application. Well-dispersed $TiO_{2-x}N_x$[31] Au/TiO_2,[32] Cu_2O,[33] AgBr,[34] BiOI,[35] *etc.* supported on BN have been already obtained with enlarged specific surface area, showing remarkable synergetic effect for the improvement of photocatalytic performance under visible light irradiation. Meanwhile, the pure BN is known as an insulator with quite wide band gap (5–6 eV),[36] but the band structures of BN are tunable by introducing impurity defects and vacancy.[36,37] Therefore, 2D BN nanosheets with tunable band structure can achieve an optimized band alignment with the photocatalyst, which offer a unique opportunity to overcome the easy recombination rate of the photo-generated electron–hole pairs, serving as the high photo-generated carrier transport way for high-performance degradation toward the target pollutants. BN modified Ag_3VO_4,[36] ZnO,[38] and CdS[39] were designed with an enlarged interaction on the curled BN surface and demonstrated a efficient charge transfer and separation processes between BN and the semiconductor, enhancing the corresponding photocatalytic activity. More interestingly, Weng *et al.*[40] found that band gaps of BN could be tuned by chemically functionalized (002) plane edges, which exhibited wide-spectrum light absorptions in both UV and visible light ranges, acting as an inorganic sensitizer to induce the visible light response of TiO_2 for a high level of photocatalytic activity toward oxidative decomposition. Hence, BN can be engineered as a support with an optimized band alignment with the photocatalyst for the improvement of photocatalytic activity.

Motivated by the band-gap tailoring strategy, herein, we have designed an *in situ* one-step method for preparation of the 3D WO_3/BN nanocomposites with highly-dispersed WO_3 particles loaded on the defective graphene-like BN nanosheets, which was different from our previous study just by the simple physical mixture of BN and WO_3 but with severe agglomeration.[41] In this study, the spatial confinement effects of BN nanosheets helped the formation of ultrasmall WO_3 nanoparticles. In addition, the randomly oriented WO_3 nanoparticles, in turn, acted as a spacer and protective layer to prevent the severe agglomeration of BN, thus contributing to a large specific surface area,[42,43] which provide more active sites for target pollutant adsorption. Besides, WO_3 with small band gap energy that can be excited by visible light, and graphene-like BN with tailored band gap can achieve an optimized band alignment with WO_3, which was beneficial for charge transport and electron–holes separation. Then, the as-prepared WO_3/BN was employed for systematical study of the photocatalytic degradation performance under visible light illumination with Rhodamine B (RhB) and Ciprofloxacin (CIP) as target pollutants. The optimal WO_3/BN sample with the mass ratio of 20% WO_3 exhibited the highest photocatalytic activity, which could degrade ~92% of RhB and exhibited excellent degradation efficiency toward CIP under visible light irradiation. In addition, ESR and the radical trapping experiments were carried out and the possible reaction mechanism for the improved photocatalytic performance was also proposed.

2. Experimental

2.1 Preparation of the photocatalysts

The WO_3/BN nanocomposites were prepared by a simple *in situ* one-step calcination method. Typically, 1.2003 g boric acid and 13.9899 g urea with the molar ratio of 1 : 12 were dissolved in 40 mL of ultrapure water, after that, 0.0163 g ammonium tungstate hydrate was added into the above solution and dissolved. Then, the mixed solution was stirred and dried at 65 °C to obtain a precursor. The obtained precursor was put into the alumina crucible, and heated in a tube furnace to 900 °C within 3 h, and then the temperature was kept for 2 h under N_2 atmosphere. The as-prepared product was defined as 3% WO_3/BN. The WO_3/BN nanocomposites with other mass ratio of 9%, 20%, and 30% were fabricated by a similar procedure. The pure graphene-like BN was synthesized by the same method without ammonium tungstate hydrate.

2.2 Characterization of the photocatalysts

The crystalline phases of WO_3/BN nanocomposites were detected using X-ray diffraction (XRD) on Bruker D8 diffractometer under Cu Kα radiation ($\lambda = 1.5418$ Å) in the scope of $2\theta = 10$–$80°$. X-Ray photoelectron spectroscopy (XPS) analysis was carried out on an ESCALab MKII X-ray photo-electron spectrometer adopting Mg Kα radiation. The transmission electron microscopy (TEM) images were picked up with a JEOL-JEM-2010 (JEOL, Japan) performed at 200 kV. An energy-dispersive X-ray spectroscope (EDS) was implemented to determine the chemical composition using an acceleration voltage of 10 kV. Ultraviolet visible (UV-Vis) diffuse reflection spectra (DRS) were conducted on an UV-Vis spectrophotometer (Shimadzu UV-2450, Japan) in the scope of 200–800 nm with $BaSO_4$ as reflectance standard substance. The Fourier transform infrared spectra (FT-IR) of the catalysts were measured using Nicolet Nexus 470 spectrometer. The photoluminescence (PL) spectra of the catalysts were collected on a QuantaMaster & TimeMaster Spectrofluorometer with the excitation wavelength of 325 nm. Photocurrents and electrochemical impedance spectroscopy (EIS) were recorded on an electro-chemical workstation (CHI 660B, Chen hua Instrument Company, Shanghai, China). X-band ESR spectra were recorded at ambient temperature on a JES FA200 spectrometer, with the settings as follows: center field, 336.496 mT; sweep width, 5 mT; microwave frequency, 9.5 GHz; modulation frequency, 100 kHz; power, 0.998 mW.

2.3 Photocatalytic experiments

The photocatalytic activity of the as-fabricated WO_3/BN was assessed by degrading the organic pollutant of RhB and CIP under the radiation source of a 300 W Xe lamp with a 400 nm cutoff filter. For each experiment, 5 mg photocatalyst was added to 50 mL RhB or CIP solution (10 mg L^{-1}) in a Pyrex photocatalytic reactor. Before irradiation, the mixture was magnetically stirred for 0.5 h in the dark to ensure the achievement of absorption/desorption equilibrium between the catalyst and pollutants. Moreover, all experiments were conducted at 30 °C with constant stirring and O_2 supply. During irradiation, 4 mL suspension was taken out every 1 h, and then centrifuged (13 000 rpm, 3 min) to separate the photocatalyst powders. The RhB and CIP concentration of the filtrates were measured by a UV-Vis spectrophotometer (UV-2450, Shimadzu) at the maximal absorbance wavelength of 553 nm. The following formula was used to obtain the photocatalytic degradation efficiency (E) of pollutants:

$$E = \left(1 - \frac{C}{C_0}\right) \times 100\% = \left(1 - \frac{A}{A_0}\right) \times 100\%$$

where C is the concentration of the solution suspension at reaction time t, and A is the corresponding values of absorbancy; C_0 is the adsorption/desorption equilibrium concentration of solution suspension, and A_0 is the corresponding values of absorbancy.

2.4 Photoelectrochemical measurements

In order to investigate the transition of photo-generated electrons, WO_3/BN electrodes were prepared. The photocurrents were measured in a standard three-electrode system, a platinum wire was employed as the counter electrode and one indium-tin oxide glass (ITO) was employed as the working electrode while a saturated Ag/AgCl electrode was used as the reference electrode. 5.0 mg sample powder was dispersed ultrasonically in 1.0 mL of ethylene glycol, and 20 μL of the resulting colloidal dispersion (5 mg mL^{-1}) was drop-cast onto a piece of ITO slice with a fixed area of 0.5 × 1 cm^2 and dried under the infrared lamp to form the sample modified ITO electrode (denoted as ITO/WO_3/BN). All the photocurrent measurements were performed at a constant potential of 0 V (*vs.* saturated Ag/AgCl). The supporting electrolyte solution of photocurrent measurements was phosphate buffered saline (0.1 mol L^{-1}, pH = 7.0). A 500 W Xe arc lamp equipment was utilized as the light source. The Nyquist plots were recorded from 100 MHz to 100 kHz frequency range. It was performed in a 0.1 M KCl solution containing 5 mM $Fe(CN)_6^{3-}$/$Fe(CN)_6^{4-}$. All electrochemical measurements above were taken at sunless conditions.

3. Results and discussion

3.1 Structure and morphology characterization

Fig. 1 shows the XRD patterns of the as-prepared WO_3/BN nanocomposites with different WO_3 contents. From those XRD patterns, it was clearly seen that the patterns of all the

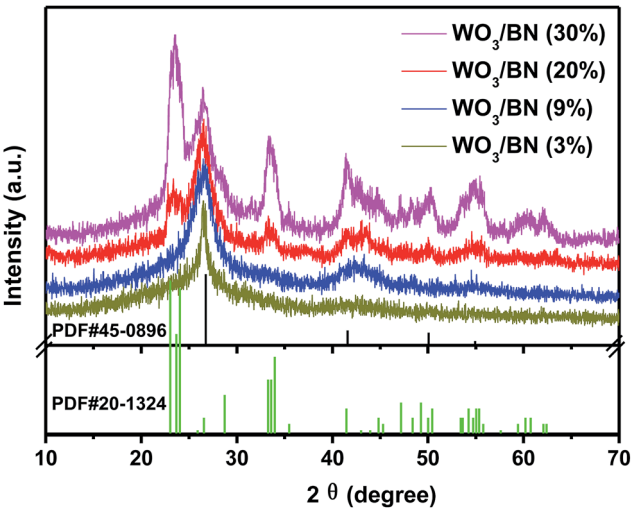

Fig. 1 XRD patterns of WO_3/BN nanocomposites.

synthesized WO_3/BN samples were combined by the diffraction peaks of both WO_3 and graphene-like BN. The diffraction peak at 26.7°, 41.6° and 50.1° can be attributed to the (002), (100) and (102) plane of the BN (JCPDF#45-0896). While the diffraction peaks at about 23.1°, 23.7°, 24.1°, 28.8°, 33.3°, 33.6°, 34.0°, 41.5°, 47.2°, 49.3°, 50.5°, 54.3°, 55.1° and 55.4° can be ascribed to (001), (020), (200), (111), (021), (201), (220), (221), (002), (400), (112), (041), (401) and (420) plane of the WO_3 (JCPDF#20-1324). On the other hand, as the increasement of WO_3 content in the nanocomposites, the peaks get strong.

The elemental composition and valence on the surface of WO_3/BN were further investigated by XPS analysis. In the full spectrum of 20% WO_3/BN nanocomposite (Fig. S1†), the element of W, O, B, and N are all observed. In addition, the C 1s peak appears at 284.8 eV is ascribed to the existence of carbon on the surface of nanocomposite, which is caused by the contamination during the measurement.[44,45] For the high resolution spectra of W 4f (Fig. 2A), the peaks locating at 35.5 eV and 37.7 eV are in accordance with the binding energies of W 4f7/2 and W 4f5/2 of W^{6+} respectively.[46,47] In O 1s spectrum (Fig. 2B and C), the peak at 532.5 eV belongs to the pure BN. The other O 1s peak at 530.3 eV is associated with the O^{2-} in the WO_3.[16] Fig. 2D shows B 1s spectrum, and the peak at 190.6 eV is attributed to the stretching vibration of B–N bond.[36] As for N 1s (Fig. 2E), the peak at 398.2 eV is due to N^{3-} in graphene-like BN.[29] Compared with the monomers, the position of all the peaks of WO_3/BN nanocomposites comes with a faint shift, which demonstrates the interaction between WO_3 and graphene-like BN. This interaction allows for the charge transfer between WO_3 and graphene-like BN, promoting the separation of photo-generated e^-–h^+ pairs, and subsequently increasing the photocatalytic efficiency of the nanocomposites.

The morphology of the pure WO_3, graphene-like BN and 20% WO_3/BN were investigated by SEM and TEM, respectively (Fig. 3). The pure WO_3 (Fig. 3A and E) presents a square block structure with a side length of about 90–120 nm, and the pure graphene-like BN (Fig. 3B and F) is consisted of thin film layer

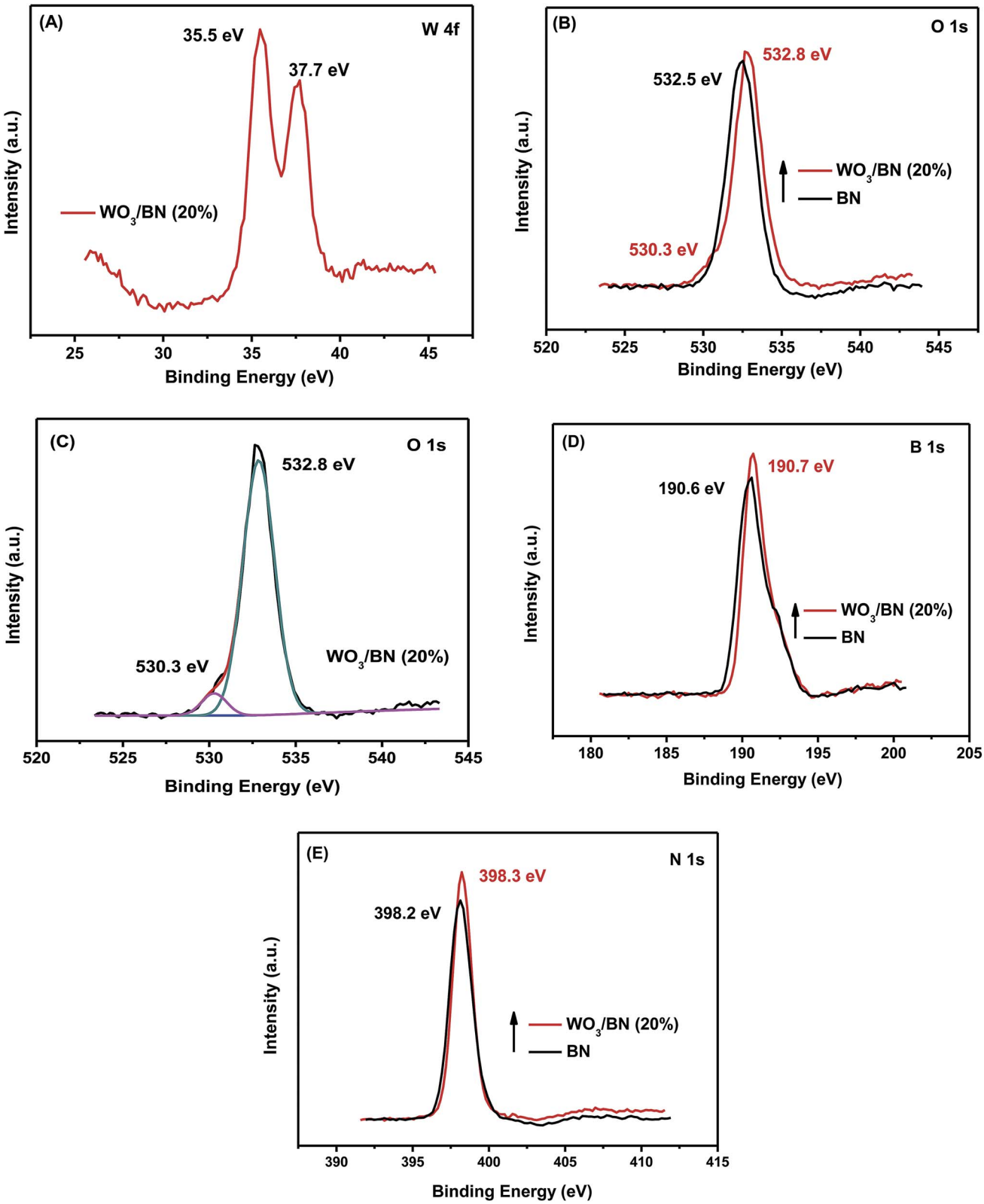

Fig. 2 High resolution XPS spectra of the samples: (A) W 4f, (B and C) O 1s, (D) B 1s, (E) N 1s of 20% WO_3/BN nanocomposite and BN.

with a very large surface. Fig. 3C and G shows the interface structure between WO_3 and graphene-like BN of the 20% WO_3/BN nanocomposite. Clearly, WO_3 is attached to the surface of graphene-like BN layers tightly and homogeneously. The interaction force between WO_3 and graphene-like BN is so strong that ultrasonication treatment cannot destroy the structure. As

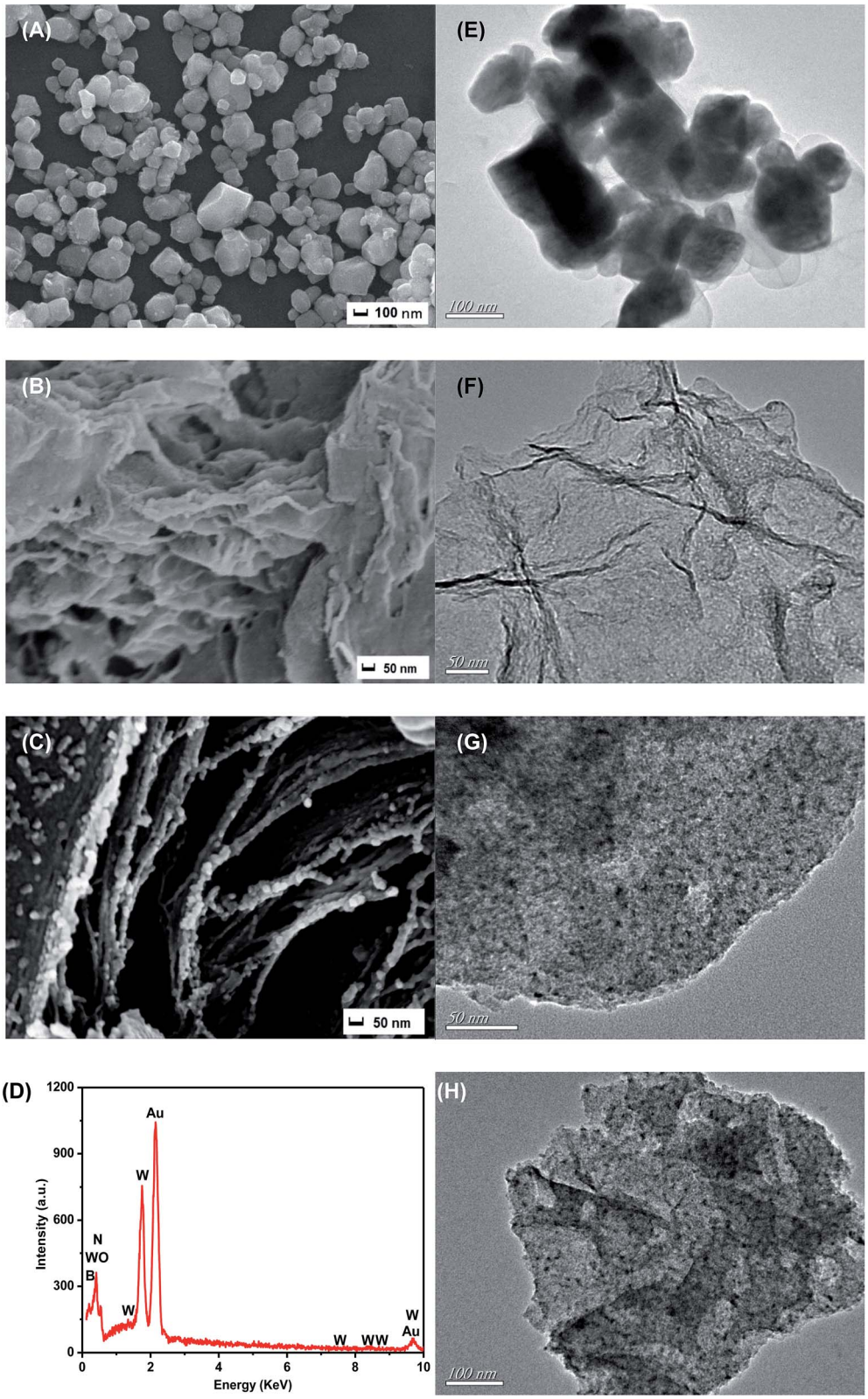

Fig. 3 SEM images of the samples: (A) WO_3, (B) graphene-like BN, (C) 20% WO_3/BN nanocomposite, (D) EDS of 20% WO_3/BN nanocomposite. TEM images of the samples: (E) WO_3, (F) graphene-like BN, (G) 20% WO_3/BN nanocomposite, (H) 30% WO_3/BN nanocomposite.

shown in EDS pattern (Fig. 3D), the elements of B, N, W and O can be detected, which further certifies the successful synthesis of the WO_3/BN nanocomposites. Fig. 3H shows the TEM image of 30% WO_3/BN nanocomposite, and there were no significant differences with 20% WO_3/BN shown in Fig. 3G. In addition, the HRTEM of the 20% WO_3/BN nanocomposite, consistent with

the EDS maps exhibited a homogeneous distribution of B, N, W and O elements over the entire nanocomposites (Fig. S2†). While, it should be noted that the homogeneous interfaces between the WO_3 and BN nanosheets have a high possibility to promote the separation of photo-induced electrons and holes, which are favorable for the improvement of photocatalytic performance.

Meanwhile, N_2 sorption–desorption isotherm (Fig. S3†) was employed to determine surface area of the photocatalysts. The surface areas were estimated to be 10.15 $m^2 g^{-1}$, 21.10 $m^2 g^{-1}$, 30.25 $m^2 g^{-1}$, 34.09 $m^2 g^{-1}$ and 32.89 $m^2 g^{-1}$ for WO_3, 3% WO_3/BN, 9% WO_3/BN, 20% WO_3/BN and 30% WO_3/BN, respectively. The WO_3/BN nanocomposites had nearly 2–3.5 times larger surface areas than that of WO_3 which could supply adequate quantity of active sites and offer more photocatalytic reaction centers for the targets, and was beneficial for the improvement of the photocatalytic performance.

3.2 Optical properties

The structure of graphene-like BN and the influence of the introduction of WO_3 on the surface groups of graphene-like BN were further explored by FT-IR analysis. And the FT-IR spectra of pure WO_3, graphene-like BN and WO_3/BN nanocomposites with different contents are presented in Fig. 4. The strong broad absorption band at about 3400–3450 cm^{-1} can be attributed to the stretching vibrations of –OH groups, bending vibrations of adsorbed molecular water.[48,49] For pure WO_3, two characteristic absorption peaks at 825 and 777 cm^{-1} can be observed, which are ascribed to the stretching vibration of the bridging oxygen atoms in O–W–O.[50] In pure graphene-like BN, the absorption band at 1387 cm^{-1} belongs to the in plane B–N stretching vibration, which is accordance with the sp^2 replacement of graphene-like BN.[42,51] And the peak at 798 cm^{-1} can be assigned to the out-of-plane bending vibrations of the B–N–B bond.[42] As for WO_3/BN nanocomposites, the peak of WO_3 at 825 cm^{-1} cannot be observed, and it may be ascribed to the existence of graphene-like BN. And the position and intensity of the absorption band at 798 cm^{-1} is slightly changed with the increase of WO_3, which indicates there may have an interaction between WO_3 and graphene-like BN in the material.[52]

DRS experiment was carried out to estimate the optical properties of the as-prepared WO_3/BN, and the result is exhibited in Fig. 5. Apparently, with the increasement of WO_3 content, the absorption of WO_3/BN nanocomposites in the visible light is significantly enhanced when compared with graphene-like BN and WO_3, respectively. In addition, the absorption edge presents a remarkable red-shift when compared to pure graphene-like BN, and the nanocomposites can absorb light in the full optical spectrum from 200 nm to 800 nm, promoting the visible light availability and consequently leading to enhancement of the photocatalytic efficiency.

PL experiment was also carried out to monitor the separation/recombination of charge-carriers generated in pure graphene-like BN and WO_3/BN nanocomposites. PL is associated to the emission of photons caused by electron–hole recombination. Therefore, a weaker intensity of the PL indicates a lower recombination efficiency of electrons and holes. Fig. 6 shows the PL spectra of pure graphene-like BN and WO_3/BN nanocomposites under the excitation wavelength of 325 nm. Clearly, with the increasing contents of WO_3, the PL intensities of the WO_3/BN nanocomposites decreased gradually, which are much lower than that of pure graphene-like BN. The result proves that the recombination of electron–hole pairs is restrained over the WO_3/BN catalysts, which is beneficial to improve the photocatalytic activity of the photocatalyst.

3.3 Electrochemical properties

To further investigate the separation and transfer efficiency of the photo-generated electrons and holes, photocurrents of WO_3/BN nanocomposites under visible light irradiation were detected for four on–off cycles. From Fig. 7, the current intensity rises to a steady value when the light on, and rapidly decreases to the dark current value when the light off. At the moment of

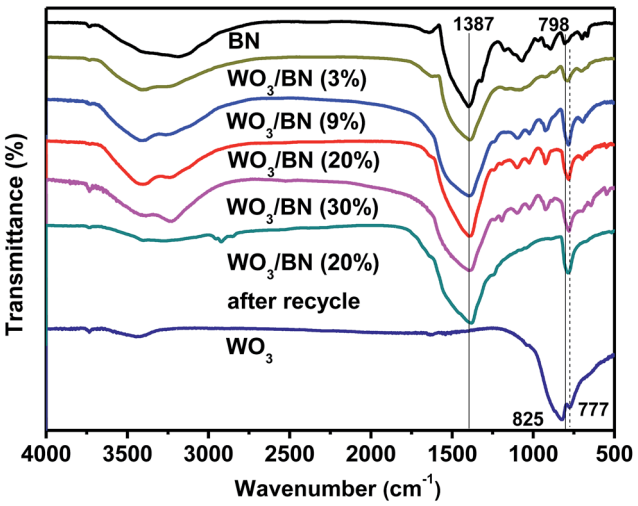

Fig. 4 FT-IR spectra of WO_3/BN nanocomposites with different contents of WO_3.

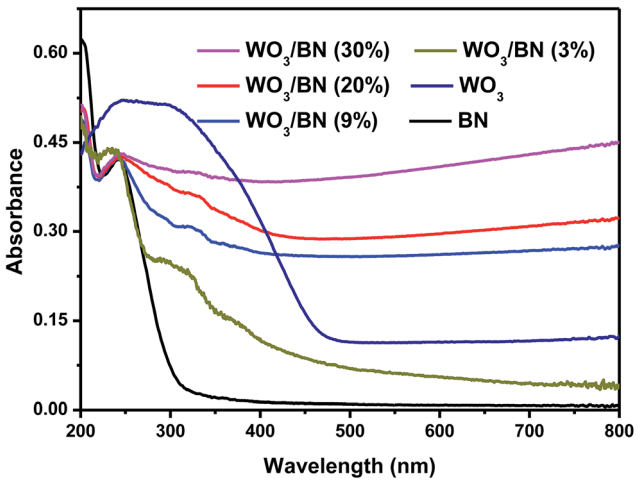

Fig. 5 UV-Vis diffuses reflectance spectra of WO_3, graphene-like BN and WO_3/BN nanocomposites.

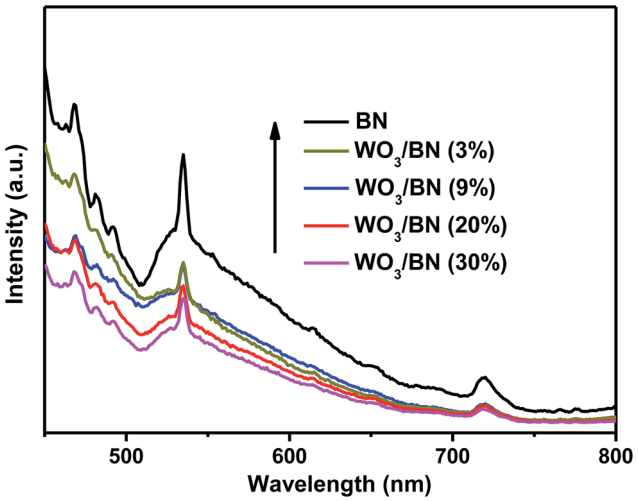

Fig. 6 PL spectra of the as-prepared pure graphene-like BN and WO_3/BN nanocomposites.

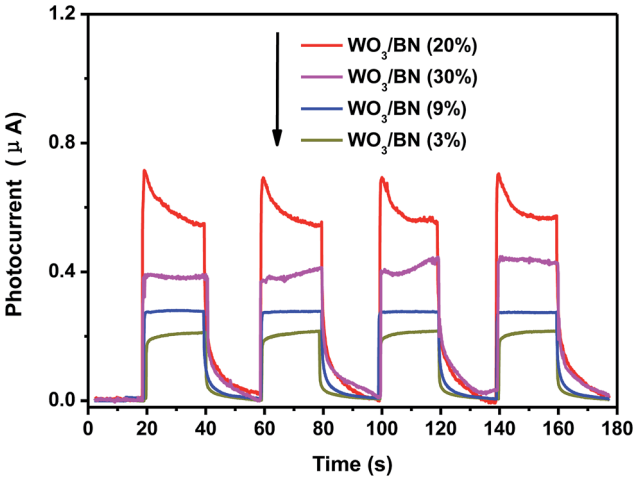

Fig. 7 Transient photocurrent response for the WO_3/BN nanocomposites in PBS (pH = 7.0) aqueous solution under visible light irradiation.

both light on and light off, the changes of currents are almost vertical, indicting the charge transport rates in the as-fabricated catalysts are very fast. Among all of these materials, the 20% WO_3/BN nanocomposite exhibits the highest photocurrent response, suggesting the highest separation efficiency and longest lifetime of the photo-generated electrons and holes in 20% WO_3/BN nanocomposite. The result further provides valid evidence that the homogeneous dispersion of WO_3 on graphene-like BN can accelerate the separation and transfer of charge carriers in the interfacial surface of WO_3/BN nanocomposites, which is considered to the contribution to the enhancement of the photocatalytic activity.

Subsequently, EIS measurement was applied to explore the resistance of charge transfer in the catalysts. The Nyquist circle in the high frequency range corresponds to the charge-transfer resistance, and the smaller circle means the lower resistance of charge transfer between the interfacial surfaces. As can be seen in Fig. 8, the semicircle of 20% WO_3/BN nanocomposite is much smaller compared to that of bare graphene-like BN. The result demonstrates that the introduction of WO_3 to graphene-like BN can dramatically reduce the interfacial charge transfer resistance and enhance the separation of photo-generated electron–hole pairs, which then bring in a remarkably improvement of photocatalytic activity. The results are consistent with the PL and photocurrent experiments.

3.4 Photocatalytic efficiency of the nanocomposites

The photocatalytic activities of the as-prepared WO_3/BN nanocomposites were evaluated by degrading RhB under visible light illumination. Fig. 9A demonstrates a comparison between the photocatalytic performances of WO_3/BN nanocomposites with different contents of WO_3. Obviously, after irradiation for 6 h, RhB could not be degraded in the absence of catalyst suggesting that the self-degradation of RhB could be neglected. After visible-light irradiation for 6 h, the photocatalytic degradation efficiencies of RhB were estimated as 9%, 49%, 84%, 92% and 70% for WO_3, 3% WO_3/BN, 9% WO_3/BN, 20% WO_3/BN and 30% WO_3/BN, respectively. We found that the photocatalytic activity gradually increased with the content of WO_3 increased from 3% to 20%, and decreased with the further increasement of the WO_3 concentration to 30%. Among all these materials, 20% WO_3/BN catalyst presented the highest photocatalytic activity. With visible light irradiating for 6 h, the degradation rate of RhB could reach about 92%, about 10.2 times higher than that of pure WO_3. For comparison, the photocatalytic performance of 20% WO_3/BN and graphene-like BN catalyst without visible light illumination were evaluated to detect the importance of light in the reaction, respectively (Fig. 9B). And in this case, BN nanosheets and the nanocomposites have the great absorption toward RhB in dark, but with negligible degradation. Therefore, the photocatalytic activity will be enhanced only in the presence of WO_3/BN catalyst with light irradiation. Noting that the

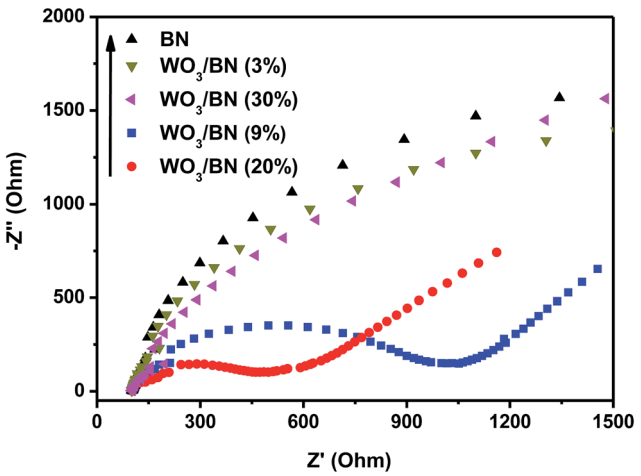

Fig. 8 EIS of the pure graphene-like BN and WO_3/BN nanocomposites in a 0.1 M KCl solution containing 5.0 mM $Fe(CN)_6^{3-}$/$Fe(CN)_6^{4-}$.

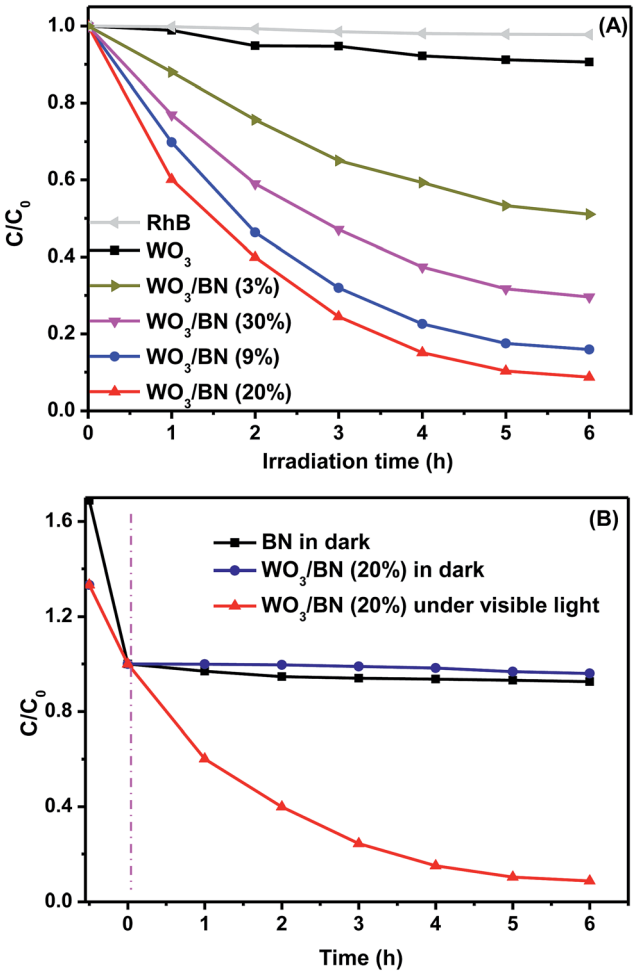

Fig. 9 (A) Photocatalytic activities of WO_3/BN nanocomposites with different contents by degrading RhB. (B) Photocatalytic activities of 20% WO_3/BN (in dark and under visible light) and graphene-like BN (in dark) by degrading RhB.

as-synthesis nanocomposites combining WO_3 (good photocatalyst) with graphene-like BN (has strong adsorption ability) led to a great improvement of photocatalytic efficiency that only thimbleful of catalyst (5 mg) could deal with 50 mL RhB solution (10 mg L^{-1}), greatly improving the utilization of the catalyst. Furthermore, from Fig. 6 of the FT-IR spectrum, the 20% WO_3/BN nanocomposite after using for RhB degradation remains unchanged compared with the one before degradation, which demonstrates that the photocatalyst is stable during the degradation process of RhB.

In addition, the repeatability is also an important factor for evaluation of the photocatalytic activity. The photocatalytic activity of the as-prepared 20% WO_3/BN nanocomposite still maintained a high level (~80.6%), even after 5 cycles for RhB degradation (Fig. S5†). Meanwhile, the XPS analysis of 20% WO_3/BN after photocatalytic reactions was also carried out (Fig. S6†), the binding energy was still maintained at their original state, which confirmed the stability of the WO_3/BN nanocomposites for RhB degradation under visible light irradiation.

The pseudo-first-order reaction model was adopted to explore the kinetics of RhB degradation by the WO_3/BN catalyst. As shown in Fig. 10A and B, the corresponding $\ln(C_0/C)$ plot presents a wonderful linearity, indicating that the photodegradation of RhB under visible light in the presence of WO_3/BN nanocomposites fits the first-order kinetics well. The 20% WO_3/BN nanocomposite displays the highest photocatalytic reaction rate under the visible light illumination and the corresponding reaction rate constant can reach to 0.28 min^{-1}.

Meanwhile, it should be noted that the anions, such as Cl^-, SO_4^{2-}, CO_3^{2-} in the natural water have an effects on the photocatalytic activity of WO_3/BN sample. Herein, the photocatalytic degradation of RhB (10 mg mL^{-1}) in the presence of anions, such as Cl^-, SO_4^{2-}, CO_3^{2-}, with the concentration of 100 mg mL^{-1} were carried out, respectively. The result (Fig. S4†) shows that the presence of anion in the system led to a decline of photocatalytic activity, we speculated that the species like Cl^-, SO_4^{2-}, CO_3^{2-}, are likely to retard the rates of oxidation of RhB by competing for the oxidizing radicals or by blocking the active sites of the WO_3/BN. However, systematic experiments and the effect mechanism should be further studied.

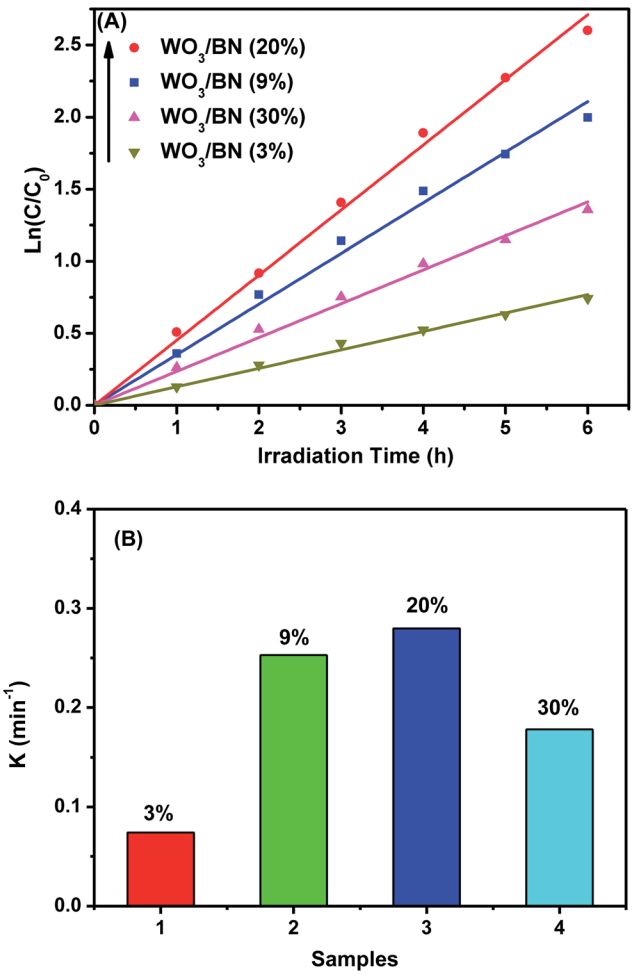

Fig. 10 (A) The first-order kinetics of WO_3/BN nanocomposites with different contents by degrading RhB, (B) the reaction rate constant of RhB with WO_3/BN nanocomposites.

CIP, as a representative colorless broad-spectrum antibiotic agent, can cause multiple negative influences. Therefore, it is very important for the CIP removal and CIP is chosen to evaluate the photocatalytic activity of the WO_3/BN nanocomposites. As shown in Fig. 11, the result revealed 75% CIP could be photo-degraded in the presence of WO_3/BN nanocomposites. The results imply that WO_3/BN is a kind of efficient photocatalysts which can also be applied to antibiotics pollution treatment.

3.5 Schematic illustration of WO_3/BN nanocomposites

As is known to all, superoxide radical ($O_2^{\bullet -}$), hydroxyl radical ($^{\bullet}OH$) and hole (h^+) are the most common reactive species acting in a photocatalytic reaction. In this work, several control experiments were carried out to explore the free radicals produced in the reaction process over 20% WO_3/BN nanocomposite. During the experiments, ethylene diamine tetraacetic acid disodium (2Na–EDTA) was introduced as holes radical scavenger, N_2 was adopted as superoxide radical scavenger, and *tert*-butanol (*t*-BuOH) was used to quench hydroxyl radical.[53] As described in Fig. 12, the degradation efficiency of RhB is 79.3% without the use of scavenger. When 2Na–EDTA and N_2 are added to the solution, the degradation efficiency is significantly reduced to 36.4% and 38.8%, respectively. Furthermore, the addition of *t*-BuOH only reduces the degradation efficiency to 65.0%. The result suggests that the photocatalytic activity of WO_3/BN is greatly inhibited by 2Na–EDTA and N_2, while slightly suppressed by *t*-BuOH. And we also demonstrates that $O_2^{\bullet -}$, h^+ and $^{\bullet}OH$ are the active species in the photocatalytic degradation reaction, while $O_2^{\bullet -}$ and h^+ play a relatively important role in the process.

In order to further ascertain the active species in the photocatalytic reaction process, the ESR spin-trap technique was applied. As presented Fig. 13A, the characteristic signals of $O_2^{\bullet -}$ (with the intensity ratio 1 : 1 : 1 : 1) are observed in WO_3/BN under visible light irradiation, while no such signals appear in dark. Fig. 13B shows that the WO_3/BN can generate $^{\bullet}OH$ (with

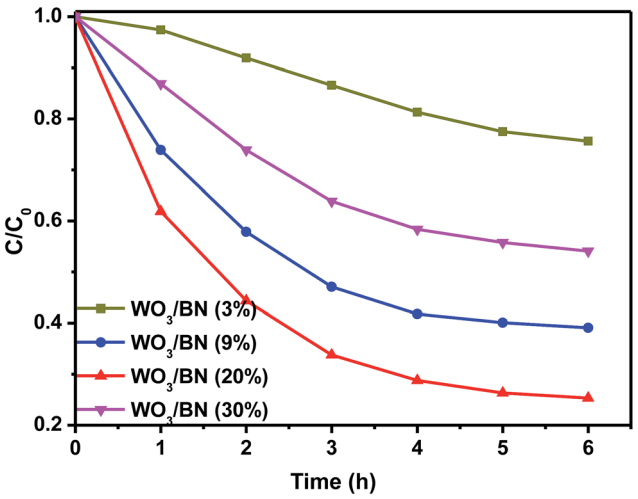

Fig. 11 Photocatalytic activities of WO_3/BN nanocomposites with different contents by degrading CIP.

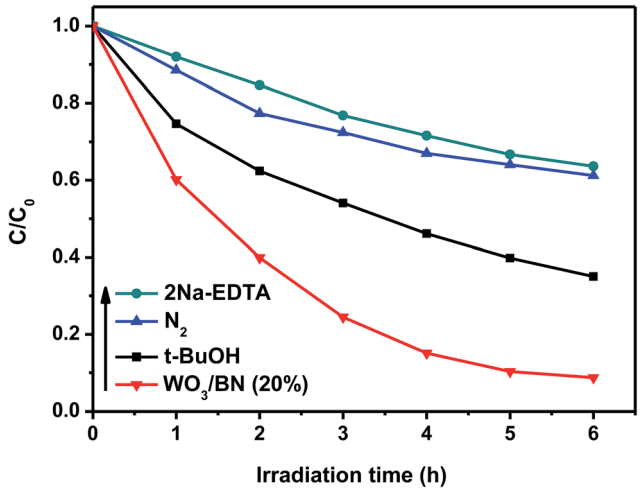

Fig. 12 Comparison of photo-degradation activities on 20% WO_3/BN nanocomposite with or without 2Na–EDTA, N_2 and *t*-BuOH under visible light illumination.

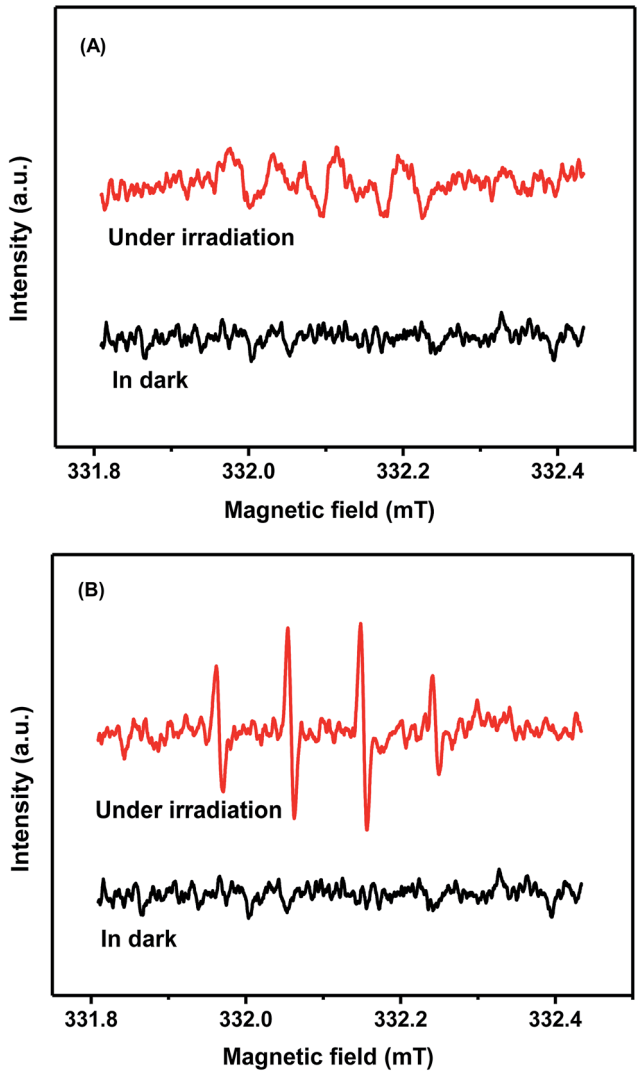

Fig. 13 The spin-trapping ESR spectra of DMPO–$O_2^{\bullet -}$ in methanol (A) and DMPO–$^{\bullet}OH$ in water (B) using 20% WO_3/BN under visible light irradiation.

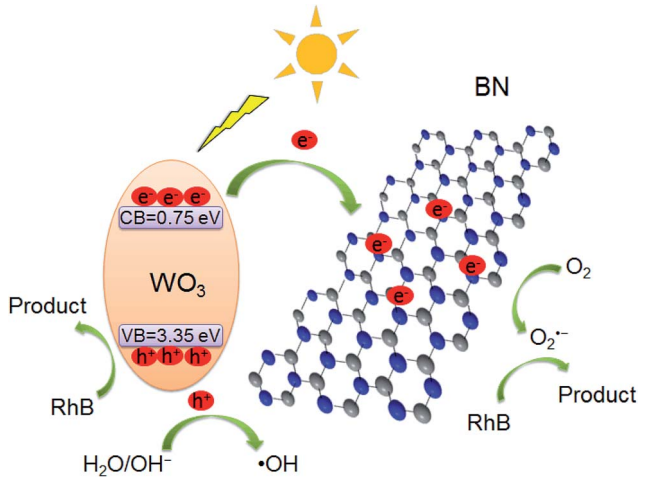

Fig. 14 Possible mechanism for RhB degradation by WO_3/BN nanocomposites during the photocatalytic reaction.

the intensity ratio 1 : 2 : 2 : 1) with light irradiation, but it cannot generate any characteristic peaks of $^{\bullet}OH$ without light illumination. These experimental results demonstrate that the active species of $O_2^{\bullet-}$ and $^{\bullet}OH$ are actually formed in the process of photocatalytic reaction, which is consistent with the radical trapping experiment.

Based on the above experimental results, a possible reaction mechanism for the significant photocatalytic activity enhancement of WO_3/BN was proposed. As described in Fig. 14, under visible light irradiation, the electrons on the valence band (VB) of WO_3 can be excited to the conduction band (CB) to generate electron–hole pairs. From DRS analysis, the introduction of WO_3 to the graphene-like BN can greatly improve the absorption of the material in visible light region, which is highly expected to improve the visible light-use efficiency. According to previous reports, graphene-like BN can work as a kind of surface passivation material to alter the behavior of photo-generated electron.[54,55] Therefore, due to the existence of the interface, the photo-generated electron can transfer from WO_3 to graphene-like BN and the efficient separation of electron–hole is realized,[32,33,35] which is in consistent with the result of PL, photocurrent and EIS analysis. Moreover, graphene-like BN owns a very large surface area, which can offer numerous active reaction sites and is beneficial for RhB to be absorbed around the photocatalyst as well. From the radical trapping experiment and ESR analysis, the photo-generated electron collected by graphene-like BN can be captured by O_2 on the surface of WO_3/BN catalysts to generate $O_2^{\bullet-}$ radicals, and the photo-induced holes on the VB of WO_3 can react with surface-absorbed H_2O or OH^- to form the hydroxyl $^{\bullet}OH$. These radicals play very important roles as active species in the photocatalytic degradation of RhB. Therefore, the WO_3/BN nanocomposites exhibit an enhancement of the photocatalytic performance.

4. Conclusion

In conclusion, the WO_3/BN nanocomposites have been successfully fabricated by a simple *in situ* one-step calcination method. The WO_3 was well-attached to the graphene-like BN so that a tight contact interface between the two materials has been successfully established. And the 20% WO_3/BN catalyst presented the highest photocatalytic activity, which could degrade ~92% of RhB under visible light illumination. The PL, photocurrent and EIS results presented that 20% WO_3/BN nanocomposite possessed a lower electron–hole recombination, higher electron–hole separation and smaller charge transfer resistance than that of the pure graphene-like BN. Combining with the radical trapping and ESR analyses, a possible reaction mechanism was also proposed. Owing to the synergetic interactions between WO_3 and graphene-like BN, the WO_3/BN nanocomposites has a significantly improved adsorption of visible light and efficient separation of photo-induced electron–hole pairs. As a result, the WO_3/BN catalyst presents a remarkably enhanced photocatalytic performance than that of the pure graphene-like BN. Therefore, the WO_3/BN nanocomposites have a high potential application for eliminating organic pollutants from wastewater.

Acknowledgements

The authors genuinely appreciate the financial support of this work by the National Natural Science Foundation of China (21476097 and 21476098), the Natural Science Foundation of Jiangsu Province (BK20131207 and BK20130513).

References

1 Y. H. Sang, Z. H. Zhao, M. W. Zhao, P. Hao, Y. H. Leng and H. Liu, *Adv. Mater.*, 2015, **27**, 363–369.
2 S. W. Zhang, H. H. Gao, X. Liu, Y. S. Huang, X. J. Xu, N. S. Alharbi, T. Hayat and J. X. Li, *ACS Appl. Mater. Interfaces*, 2016, **8**, 35138–35149.
3 S. W. Zhang, H. H. Gao, J. X. Li, Y. S. Huang, A. Alsaedi, T. Hayat, X. J. Xu and X. K. Wang, *J. Hazard. Mater.*, 2017, **321**, 92–102.
4 S. W. Zhang, Q. H. Fan, H. H. Gao, Y. S. Huang, X. Liu, J. X. Li, X. J. Xu and X. K. Wang, *J. Mater. Chem. A*, 2016, **4**, 1414–1422.
5 S. D. Perera, R. G. Mariano, K. Vu, N. Nour, O. Seitz, Y. Chabal and K. J. Balkus, *ACS Catal.*, 2012, **2**, 949–956.
6 R. Li, Y. F. Jia, N. J. Bu, J. Wu and Q. Zhen, *J. Alloys Compd.*, 2015, **643**, 88–93.
7 D. Q. Bi and Y. M. Xu, *J. Mol. Catal. A: Chem.*, 2013, **367**, 103–107.
8 H. Tong, S. X. Ouyang, Y. P. Bi, N. Umezawa, M. Oshikiri and J. H. Ye, *Adv. Mater.*, 2012, **24**, 229–251.
9 Y. F. Liu, W. Q. Yao, D. Liu, R. L. Zong, M. Zhang, X. G. Ma and Y. F. Zhu, *Appl. Catal., B*, 2015, **163**, 547–553.
10 J. P. Wang, H. Xu, X. F. Qian, Y. Y. Dong, J. K. Gao, G. D. Qian and J. M. Yao, *Chem.–Asian J.*, 2015, **10**, 1276–1280.
11 J. K. Gao, J. P. Wang, X. F. Qian, Y. Y. Dong, H. Xu, R. J. Song, C. F. Yan, H. C. Zhu, Q. W. Zhong and G. D. Qian, *J. Solid State Chem.*, 2015, **228**, 60–64.
12 K. Manthiram and A. P. Alivisatos, *J. Am. Chem. Soc.*, 2012, **134**, 3995–3998.

13 G. R. Bamwenda and H. Arakawa, *Appl. Catal., A*, 2001, **210**, 181–191.
14 J. Yu, L. F. Qi, B. Cheng and X. F. Zhao, *J. Hazard. Mater.*, 2008, **160**, 621–628.
15 Z. G. Zhao and M. Miyauchi, *Angew. Chem., Int. Ed.*, 2008, **47**, 7051–7055.
16 L. Y. Huang, H. Xu, Y. P. Li, H. M. Li, X. N. Cheng, J. X. Xia, Y. G. Xu and G. B. Cai, *Dalton Trans.*, 2013, **42**, 8606–8616.
17 S. Sun, W. Wang, S. Zeng, M. Shang and L. Zhang, *J. Hazard. Mater.*, 2010, **178**, 427–433.
18 D. Hidayat, A. Purwanto, W. N. Wang and K. Okuyama, *Mater. Res. Bull.*, 2010, **45**, 165–173.
19 H. Widiyandari, A. Purwanto, R. Balgis, T. Ogi and K. Okuyama, *Chem. Eng. J.*, 2012, **180**, 323–329.
20 M. Qamar, M. A. Gondal and Z. H. Yamani, *Catal. Commun.*, 2010, **11**, 768–772.
21 A. Fujii, Z. C. Meng, C. Yogi, T. Hashishin, T. Sanada and K. Kojima, *Surf. Coat. Technol.*, 2015, **271**, 251–258.
22 S. Shamaila, A. K. Sajjad, F. Chen and J. Zhang, *J. Colloid Interface Sci.*, 2011, **356**, 465–472.
23 S. A. K. Leghari, S. Sajjad, F. Chen and J. Zhang, *Chem. Eng. J.*, 2011, **166**, 906–915.
24 D. Li and H. Haneda, *J. Photochem. Photobiol., A*, 2003, **160**, 203–212.
25 G. Lu, X. Li, Z. Qu, Y. Wang and G. Chen, *Appl. Surf. Sci.*, 2008, **255**, 3117–3120.
26 J. X. Wang, J. Y. Shen, D. L. Fan, Z. S. Cui, X. M. Lü, J. M. Xie and M. Chen, *Mater. Lett.*, 2015, **147**, 8–11.
27 X. L. Fu, Y. F. Hu, T. Zhang and S. F. Chen, *Appl. Surf. Sci.*, 2013, **280**, 828–835.
28 W. W. Lei, D. Portehault, D. Liu, S. Qin and Y. Chen, *Nat. Commun.*, 2013, **4**, 1777–1783.
29 Y. M. Shi, C. Hamsen, X. T. Jia, K. K. Kim, A. Reina, M. Hofmann, A. L. Hsu, K. Zhang, H. N. Li, Z. Y. Juang, M. S. Dresselhaus, L. J. Li and J. Kong, *Nano Lett.*, 2010, **10**, 4134–4139.
30 J. T. Grant, C. A. Carrero, F. Goeltl, J. Venegas, P. Mueller, S. P. Burt, S. E. Specht, W. P. McDermott, A. Chieregato and I. Hermans, *Science*, 2016, **354**, 1570–1573.
31 D. Liu, W. Q. Cui, J. Lin, Y. M. Xue, Y. Huang, J. Li, J. Zhang, Z. Y. Liu and C. C. Tang, *Catal. Commun.*, 2014, **57**, 9–13.
32 Y. Ide, F. Liu, J. Zhang, N. Kawamoto, K. Komaguchi, Y. Bando and D. Golberg, *J. Mater. Chem. A*, 2014, **2**, 4150–4156.
33 C. J. Huang, W. Q. Ye, Q. W. Liu and X. D. Qiu, *ACS Appl. Mater. Interfaces*, 2014, **6**, 14469–14476.
34 J. J. Chen, J. X. Zhu, Z. L. Da, H. Xu, J. Yan, H. Y. Ji, H. M. Shu and H. M. Li, *Appl. Surf. Sci.*, 2014, **313**, 1–9.
35 D. Liu, Z. F. Jiang, C. Z. Zhu, K. Qian, Z. Y. Wu and J. M. Xie, *Dalton Trans.*, 2016, **45**, 2505–2516.
36 X. M. Lv, J. J. Wang, Z. X. Yan, D. L. Jiang and J. Liu, *J. Mol. Catal. A: Chem.*, 2016, **418–419**, 146–153.
37 A. Nag, K. Raidongia, K. P. S. S. Hembram, R. Datta, U. V. Waghmare and C. N. R. Rao, *ACS Nano*, 2010, **4**, 1539–1544.
38 A. Yamuna, A. Mandalam, A. Karthigaiselvi, M. Balasubramanian, B. Thiruparasakthi, S. Ravichandran and S. Mayavan, *RSC Adv.*, 2015, **5**, 69394–69399.
39 X. P. Li, F. Qi, Y. M. Xue, C. Yu, H. C. Jia, Y. H. Bai, S. Wang, Z. Y. Liu, J. Zhang and C. C. Tang, *RSC Adv.*, 2016, **6**, 99165–99171.
40 Q. H. Weng, Y. Ide, X. B. Wang, X. Wang, C. Zhang, X. F. Jiang, Y. M. Xue, P. C. Dai, K. Komaguchi, Y. Bando and D. Golberg, *Nano Energy*, 2015, **16**, 19–27.
41 H. Xu, L. Liu, Y. H. Song, L. Y. Huang, Y. P. Li, Z. G. Chen, Q. Zhang and H. M. Li, *J. Alloys Compd.*, 2016, **660**, 48–54.
42 J. Di, J. X. Xia, M. X. Ji, B. Wang, S. Yin, Q. Zhang, Z. G. Chen and H. M. A. Li, *Appl. Catal., B*, 2016, **183**, 254–262.
43 P. W. Wu, W. S. Zhu, B. L. Dai, Y. H. Chao, C. F. Li, H. P. Li, M. Zhang, W. S. Jiang and H. M. Li, *Chem. Eng. J.*, 2016, **301**, 123–131.
44 Y. P. Li, S. L. Wu, L. Y. Huang, H. Xu, R. X. Zhang, M. L. Qu, Q. Gao and H. M. Li, *J. Phys. Chem. Solids*, 2015, **76**, 112–119.
45 P. Niu, G. Liu and H. M. Cheng, *J. Phys. Chem. C*, 2012, **116**, 11013–11018.
46 P. Chatchai, Y. Murakami, S. Y. Kishioka, A. Y. Nosaka and Y. Nosaka, *Electrochim. Acta*, 2009, **54**, 1147–1152.
47 G. Lu, X. Y. Li, Z. P. Qu, Q. D. Zhao, H. Li, Y. Shen and G. H. Chen, *Chem. Eng. J.*, 2010, **159**, 242–246.
48 K. Wang, B. S. Li, B. Cheng, W. K. Ho and J. G. Yu, *Appl. Catal., B*, 2015, **176–177**, 44–52.
49 X. J. Bai, L. Wang, R. L. Zong and Y. F. Zhu, *J. Phys. Chem. C*, 2013, **117**, 9952–9961.
50 G. C. Xi, B. Yue, J. Y. Cao and J. H. Ye, *Chemistry*, 2011, **17**, 5145–5154.
51 C. J. Huang, C. Chen, M. W. Zhang, L. H. Lin, X. X. Ye, S. Lin, M. Antonietti and X. C. Wang, *Nat. Commun.*, 2015, **6**, 7698–7704.
52 Y. G. Xu, H. Xu, L. Wang, J. Yan, H. M. Li, Y. H. Song, L. Y. Huang and G. B. T. Cai, *Dalton Trans.*, 2013, **42**, 7604–7613.
53 Y. Y. Zhu, Y. F. Liu, Y. H. Lv, Q. Ling, D. Liu and Y. F. Zhu, *J. Mater. Chem. A*, 2014, **2**, 13041–13048.
54 W. B. Li, Q. Wang, L. Y. Huang, Y. P. Li, Y. G. Xu, Y. H. Song, Q. Zhang, H. Xu and H. M Li, *RSC Adv.*, 2015, **5**, 88832–88840.
55 M. Shanmugam, R. Jacobs-Gedrim, C. Durcan and B. Yu, *Nanoscale*, 2013, **5**, 11275–11282.